2. Galopeau, P. H. M., Zarka, P. & Le Quéau, D. Source location of Saturn's kilometric radiation: The Kelvin-Helmholtz instability hypothesis. *J. Geophys. Res.* **100,** 26397–26410 (1995).

3. Warwick, J. W. *et al.* Planetary radio astronomy observations from Voyager 1 near Saturn. *Science* **212,** 239–243 (1981).

4. Galopeau, P. H. M. & Lecacheux, A. Variations in Saturn's radio rotation period measured at kilometer wavelengths. *J. Geophys. Res.* **105,** 13089–13101 (2000).

5. Zarka, P. in *Planetary Radio Emissions II* (eds Rucker, H. O., Bauer, S. J. & Pedersen, B. M.) 327–342 (Austrian Acad. Sci. Press, Vienna, 1988).

6. Zarka, P. Auroral radio emissions at the outer planets: Observations and theories. *J. Geophys. Res.* **103,** 20159–20194 (1998).

7. Desch, M. D. Evidence for solar wind control of Saturn radio emission. *J. Geophys. Res.* **87,** 4549–4554 (1982).

8. Clarke, J. T. *et al.* Morphological differences of Saturn's ultraviolet aurorae and those of Earth and Jupiter. *Nature* doi:10.1038/nature03331 (this issue).

9. Wu, C. S. & Lee, L. C. A theory of terrestrial kilometric radiation. *Astrophys. J.* **230,** 621–626 (1979).

10. Galopeau, P., Zarka, P. & Le Quéau, D. Theoretical model of Saturn's kilometric radiation spectrum. *J. Geophys. Res.* **94,** 8739–8755 (1989).

11. Connerney, J. E. P., Ness, N. F. & Acuña, M. H. Zonal harmonic model of Saturn's magnetic field from Voyager 1 and 2 observations. *Nature* **298,** 44–46 (1982).

12. Galopeau, P., Ortega-Molina, A. & Zarka, P. Evidence of Saturn's magnetic field anomaly from SKR high-frequency limit. *J. Geophys. Res.* **96,** 14129–14140 (1991).

13. Galopeau, P. & Zarka, P. Reply to the comment by J. E. P. Connerney and M. D. Desch on "Evidence of Saturn's magnetic field anomaly from SKR high-frequency limit". *J. Geophys. Res.* **97,** 12291–12297 (1992).

14. Gurnett, D. A. *et al.* The Cassini radio and plasma wave science investigation. *Space Sci. Rev.* (in the press).

15. Gurnett, D. A. The Earth as a radio source: Terrestrial kilometric radiation. *J. Geophys. Res.* **79,** 4227–4238 (1974).

16. Crary, F. J. *et al.* Solar wind dynamic pressure and electric field as the main factors controlling Saturn's aurorae. *Nature* doi:10.1038/nature03333 (this issue).

17. Huff, R. L., Calvert, W., Craven, J. D., Frank, L. A. & Gurnett, D. A. Mapping of auroral kilometric radiation sources to the aurora. *J. Geophys. Res.* **93,** 11445–11454 (1988).

18. de Feraudy, H., Bahnsen, A. & Jespersen, M. in *Planetary Radio Emissions II* (eds Rucker, H. O., Bauer, S. J. & Pedersen, B. M.) 41–60 (Austrian Acad. Sci. Press, Vienna, 1988).

19. Stone, R. G. *et al.* The unified radio and plasma wave investigation. *Astron. Astrophys. Suppl. Ser.* **92,** 291–316 (1992).

20. Wenzel, K. P., Marsden, R. G., Page, D. E. & Smith, E. J. The Ulysses mission. *Astron. Astrophys. Suppl. Ser.* **92,** 207–219 (1992).

21. Imhof, W. L. *et al.* The dependence of AKR production on the intensity and energy spectra of auroral bremsstrahlung. *J. Geophys. Res.* **108,** doi:10.1029/2002JA009274 (2003).

22. Knight, S. Parallel electric fields. *Planet. Space Sci.* **21,** 741–750 (1973).

23. Cowley, S. W. H. & Bunce, E. J. Origin of the main auroral oval in Jupiter's coupled magnetosphere-ionosphere system. *Planet. Space Sci.* **49,** 1067–1088 (2001).

Competing interests statement The authors declare that they have no competing financial interests.

Correspondence and requests for materials should be addressed to W.S.K. (william-kurth@uiowa.edu).

··

A continuous-wave Raman silicon laser

Haisheng Rong[1], **Richard Jones**[1], **Ansheng Liu**[1], **Oded Cohen**[2], **Dani Hak**[2], **Alexander Fang**[1] **& Mario Paniccia**[1]

[1]*Intel Corporation, 2200 Mission College Blvd, CHP3-109, Santa Clara, California 95054, USA*
[2]*Intel Corporation, SBI Park Har Hotzvim, Jerusalem, 91031, Israel*

···

Achieving optical gain and/or lasing in silicon has been one of the most challenging goals in silicon-based photonics[1–3] because bulk silicon is an indirect bandgap semiconductor and therefore has a very low light emission efficiency. Recently, stimulated Raman scattering has been used to demonstrate light amplification and lasing in silicon[4–9]. However, because of the nonlinear optical loss associated with two-photon absorption (TPA)-induced free

carrier absorption (FCA)[10–12], until now lasing has been limited to pulsed operation[8,9]. Here we demonstrate a continuous-wave silicon Raman laser. Specifically, we show that TPA-induced FCA in silicon can be significantly reduced by introducing a reverse-biased p-i-n diode embedded in a silicon waveguide. The laser cavity is formed by coating the facets of the silicon waveguide with multilayer dielectric films. We have demonstrated stable single mode laser output with side-mode suppression of over 55 dB and linewidth of less than 80 MHz. The lasing threshold depends on the p-i-n reverse bias voltage and the laser wavelength can be tuned by adjusting the wavelength of the pump laser. The demonstration of a continuous-wave silicon laser represents a significant milestone for silicon-based optoelectronic devices.

The continuous-wave (c.w.) silicon Raman laser is constructed from a low-loss silicon-on-insulator (SOI) rib waveguide whose facets are coated with multilayer dielectric films. The front facet coating is dichroic, having a reflectivity (R_f) of ~71% for the Raman/Stokes wavelength of 1,686 nm and ~24% for the pump wavelength of 1,550 nm. The back facet has a broadband high-reflectivity coating (R_b) of ~90% for both pump and Raman wavelengths (Fig. 1a). These waveguide facet reflectivities were determined using a Fabry–Pérot resonance technique[2].

The silicon rib waveguide is fabricated on the (100) surface of an undoped SOI substrate using standard photolithographic patterning and reactive ion etching techniques. We designed the waveguide dimensions with the goal of obtaining a small cross-section for minimizing the required optical power to achieve the lasing threshold, but not so small as to cause high transmission loss. A cross-section scanning electron microscope image of a typical p-i-n waveguide is shown in Fig. 1b. The rib waveguide dimensions are: rib width (W) ~1.5 µm; height (H) ~1.55 µm; and etch depth (h) ~0.7 µm. The effective core area[13] of the waveguide is calculated to
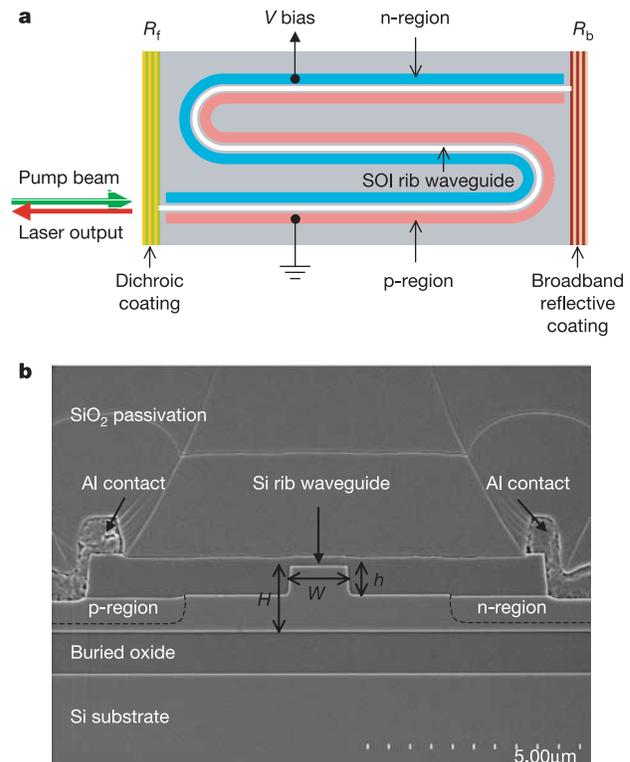

Figure 1 Silicon waveguide used in the Raman laser experiment. **a**, Schematic layout of the silicon waveguide laser cavity with optical coatings applied to the facets and a p-i-n structure along the waveguide. **b**, Scanning electron microscope cross-section image of a silicon rib waveguide with a p-i-n diode structure.

be ~1.6 μm². The waveguide was formed in an S-shaped curve with a total length of 4.8 cm and a bend radius of 400 μm (Fig. 1a). The straight sections of the waveguide are oriented along the [011] crystallographic direction.

A p-i-n diode structure was designed to reduce the nonlinear optical loss due to the TPA-induced FCA. The p-i-n structure was formed by implanting boron and phosphorus in the slab on either side of the rib waveguide (Fig. 1a, b) with a doping concentration of ~1 × 10²⁰ cm⁻³. The separation between the p- and n-doped regions was designed to be ~6 μm. Ohmic contacts were formed by depositing aluminium films on the surface of the p- and n-doped regions. This was followed by a SiO₂ passivation layer deposition. The doped regions and the metal contacts at the designed separation had negligible effect on the propagation loss of the waveguide because the optical mode is tightly confined in the waveguide. This was verified experimentally. The linear optical transmission loss of the S-bend waveguide was measured to be 0.35 dB cm⁻¹ using the Fabry–Pérot resonance technique[2].

When a reverse bias voltage is applied to the p-i-n diode, the TPA-generated electron–hole pairs can be swept out of the silicon waveguide by the electric field between the p- and n-doped regions. Thus the effective carrier lifetime, representing the lifetime of the free carrier's interaction with the optical mode in the waveguide region, reduces with increased bias voltage. This has been experimentally verified by comparing the measured nonlinear transmission of a silicon waveguide with modelling[9,14]. The measured photocurrent in the reverse-biased p-i-n diode scales with the square of the light power inside the waveguide, indicating that the charge carriers are generated by the TPA process[10]. At a reverse-bias voltage of 25 V, the effective carrier lifetime is reduced to ~1 ns compared to the free carrier lifetime of several tens of nanoseconds in ordinary silicon rib waveguides[10,11]. Before performing the lasing experiment, the single-pass c.w. Raman gain of a p-i-n silicon waveguide was measured in a pump–probe experiment[14], showing a single-pass net gain of >3 dB at a reverse-bias voltage of 25 V and a pump power of ~700 mW coupled into the waveguide.

Figure 2 is a schematic of the Raman laser experiment. A c.w. external cavity diode laser (ECDL) at 1,550 nm is amplified by an erbium-doped fibre amplifier system to produce a pump beam of up to 3 W. The pump beam passes through a polarization controller followed by a thin-film-based wavelength de-multiplexer and is coupled into the waveguide cavity by a lensed fibre through the dichroic-coated front facet. The Raman laser output and the reflected pump beam are coupled back into the lensed fibre, and separated through the wavelength de-multiplexer. The extracted laser output from the reflection port of the de-multiplexer is further filtered by a long-wavelength pass filter before being detected by a power meter or optical spectrum analyser. The coupling loss
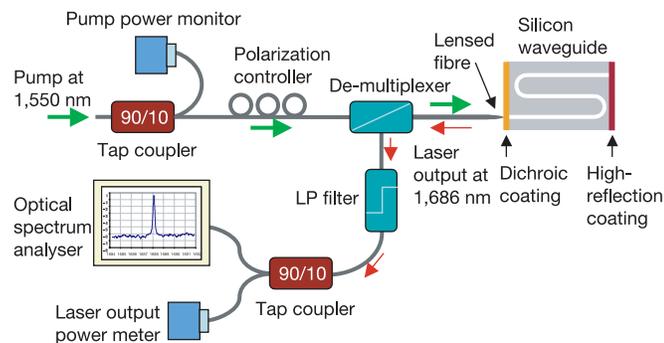
between the lensed fibre and the waveguide was measured to be ~4 dB and the insertion loss of the de-multiplexer and the long-wavelength pass filter is ~0.6 dB. The silicon chip is mounted on a thermo electric cooler and kept at a constant temperature of 25 °C.

At the pump wavelength, a low finesse cavity is formed by the low reflectivity front facet and high reflectivity back facet. This configuration allows the cavity enhancement effect[15–17] of the pump power to be used to lower the lasing threshold. When the pump laser is tuned to the resonance of the cavity, the circulating power inside the waveguide cavity is enhanced, and the effective mean internal power (I_{eff}) inside the cavity can be expressed as[18]:

$$I_{eff} = I_i \frac{1 - e^{-\alpha L}}{\alpha L} \frac{(1 - R_f)(1 + R_b e^{-\alpha L})}{(1 - \sqrt{R_f R_b} e^{-\alpha L})^2}$$

where I_i is the incident pump power (less coupling loss), R_f and R_b are the reflectivity of the front and back facet respectively, α is the absorption coefficient, and L is the waveguide length. At low power, we can estimate the power enhancement factor $M = I_{eff}/I_i$ to be ~2.2, using our experimental parameters. At high power, however, the absorption coefficient α increases owing to the TPA-induced nonlinear absorption, and M reduces accordingly.

Figure 3 plots the Raman laser output power versus the input pump power (I_i) coupled into the laser cavity depicted in Fig. 1a, at two different reverse-bias voltages applied to the p-i-n diode. In the experiment, the pump beam polarization is adjusted with a polarization controller and its wavelength is fine-tuned to the cavity resonance to take advantage of the cavity enhancement of the pump and maximize the laser output. The Raman laser frequency is 15.6 THz lower than that of the pump laser. We see from Fig. 3 that the lasing threshold reduces with increasing reverse-bias voltage. The lasing threshold is ~280 mW with a 5-V bias and ~180 mW with a 25-V bias. The lower threshold and higher laser output power with higher reverse-bias voltage are expected because the effective carrier lifetime is shorter, resulting in lower nonlinear loss and higher gain[14]. For this waveguide cavity, the total loss of the feedback mirrors ($R_f = 71\%$ and $R_b = 90\%$) at the lasing wavelength is ~2 dB, so a ~1-dB single-pass net gain is needed to reach lasing threshold. From previous measurements[14], a ~1-dB net c.w. gain is obtained at a pump power of ~400 mW with 25-V reverse bias and ~600 mW with 5-V reverse bias. Taking into account the cavity enhancement factor of ~2.2, the lasing thresholds are

Figure 2 Schematic set-up of the silicon Raman laser experiment. See main text for details.
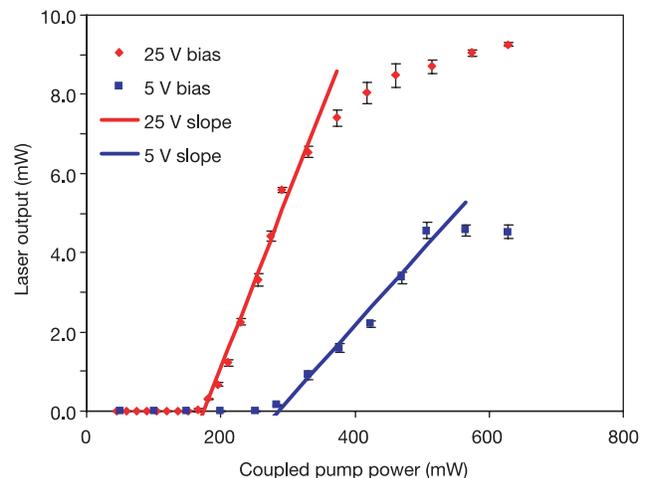
Figure 3 Silicon Raman laser output power as a function of the input pump power at a reverse bias of 25 and 5 V. The pump wavelength is 1,550 nm and the laser wavelength is 1,686 nm. The slope efficiency (single side output) is 4.3% for 25-V bias and 2% for 5-V bias. Error bars represent standard deviations.

expected to be ~182 and ~273 mW for reverse biases of 25 and 5 V, respectively, which is consistent with our measurements. The slope efficiency (single side output) above threshold is ~4.3% with a reverse bias of 25 V, and 2% with a reverse bias of 5 V. Figure 3 also shows that the laser output power begins to saturate at a pump power of >400 mW with a 25-V bias and at a pump power of >500 mW with a 5-V bias. This is primarily due to the nonlinear loss caused by the TPA-induced FCA as a consequence of the non-zero carrier lifetime of the p-i-n waveguide, reducing the net gain at higher pump powers. In addition, the cavity enhancement factor M for the pump reduces with increasing nonlinear loss, lowering the effective pump power in the cavity.

The spectrum of the laser output is measured with a confocal scanning Fabry–Pérot spectrum analyser with a free spectral range of 8 GHz and finesse of 100. Figure 4a shows the Raman laser spectrum measured at a pump power of ~400 mW and a reverse bias of 25 V. As shown, the laser has single-mode output, that is, no other cavity modes with expected mode spacing of 0.9 GHz for a 4.8-cm-long silicon waveguide cavity appear within the free spectral range (8 GHz) of the spectrum analyser. The measured linewidth of 80 MHz is limited by the resolution of the spectrum analyser. This was verified by recording the spectrum of a narrow-band laser of linewidth <1 MHz with the same spectrum analyser.
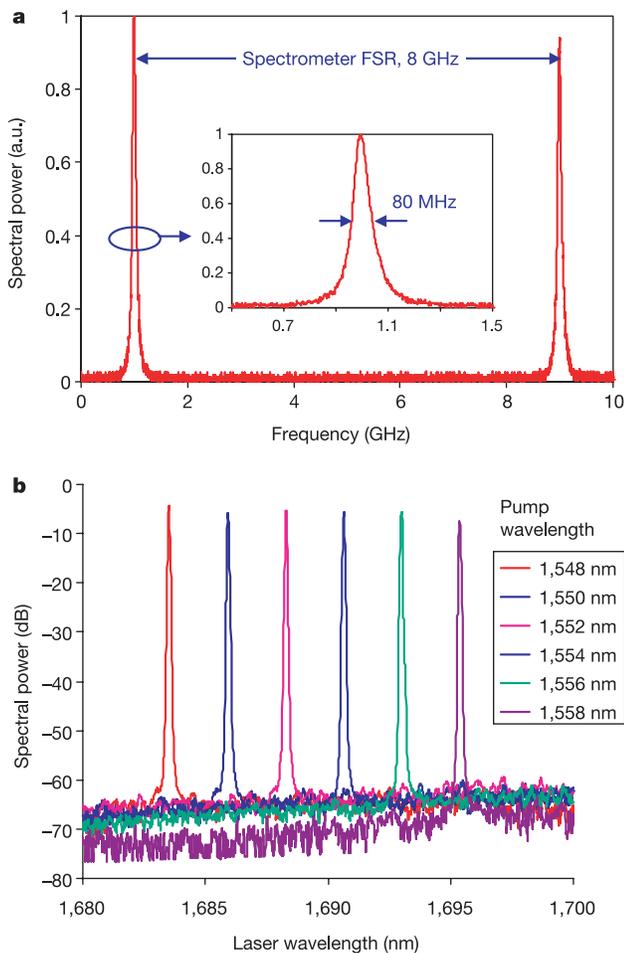
Figure 4b is a plot of the laser output spectrum measured with a grating-based optical spectrum analyser with 0.07-nm resolution at various pump wavelengths. The spectra shown were obtained by changing the wavelength of the pump laser seed (ECDL) from 1,548 to 1,558 nm in 2-nm steps. The input pump power was ~400 mW and a reverse bias of 25 V was applied to the p-i-n diode. The Raman laser output has side-mode suppression of over 55 dB and its centre wavelength corresponds to the appropriate Stokes shift for each pump wavelength. The displayed linewidth is limited by the resolution of the spectrum analyser. The small fluctuation in output power is due to the wavelength dependence of the insertion loss of the de-multiplexer, the long-wavelength pass filter, and the gain of erbium-doped fibre amplifiers.

This first demonstration of c.w. Raman lasing in silicon represents a significant milestone towards producing fully integrated monolithic photonic chips. The performance of this silicon Raman laser could be further improved by optimizing cavity mirror and cavity length design. The threshold power could be reduced by using a waveguide with smaller cross-sectional dimensions and/or by introducing a larger cavity enhancement for the pump beam. The fibre to waveguide coupling efficiency could be improved by adding a mode converter in the waveguide[19]. In addition, with optimization of the p-i-n diode design, it may be possible to further reduce the effective carrier lifetime to below 1 ns. This would reduce the saturation effect and thus increase the laser output power. The multilayer coating approach used to form the cavity mirrors could also be replaced with waveguide Bragg reflectors[20,21], ring or microdisk resonator architectures[22–25]; this could provide a platform for monolithic integration of silicon-based optoelectronics. □

1. Pavesi, L. & Gaponenko, S. (eds) *Towards the First Silicon Laser* (NATO Science Series, Kluwer, Dordrecht, 2003).
2. Reed, G. T. & Knights, A. P. *Silicon Photonics: An Introduction* (John Wiley, Chichester, UK, 2004).
3. Pavesi, L. & Lockwood, D. J. (eds) *Silicon Photonics* (Springer, Berlin, 2004).
4. Liu, A., Rong, H., Paniccia, M., Cohen, O. & Hak, D. Net optical gain in a low loss silicon-on-insulator waveguide by stimulated Raman scattering. *Opt. Expr.* **12,** 4261–4267 (2004).
5. Xu, Q., Almeida, V. & Lipson, M. Time-resolved study of Raman gain in highly confined silicon-on-insulator waveguides. *Opt. Expr.* **12,** 4437–4442 (2004).
6. Liang, T. K. & Tsang, H. K. Efficient Raman amplification in silicon-on-insulator waveguides. *Appl. Phys. Lett.* **85,** 3343–3345 (2004).
7. Boyraz, O. & Jalali, B. Demonstration of 11 dB fiber-to-fiber gain in a silicon Raman amplifier. *IEICE Elect. Expr.* **1,** 429–434 (2004).
8. Boyraz, O. & Jalali, B. Demonstration of a silicon Raman laser. *Opt. Expr.* **12,** 5269–5273 (2004).
9. Rong, H. *et al.* An all-silicon Raman laser. *Nature* **433,** 292–294 (2005).
10. Liang, T. K. & Tsang, H. K. Role of free carriers from two-photon absorption in Raman amplification in silicon-on-insulator waveguides. *Appl. Phys. Lett.* **84,** 2745–2747 (2004).
11. Rong, H. *et al.* Raman gain and nonlinear optical absorption measurement in a low loss silicon waveguide. *Appl. Phys. Lett.* **85,** 2196–2198 (2004).
12. Claps, R., Raghunathan, V., Dimitropoulos, D. & Jalali, B. Role of nonlinear absorption on Raman amplification in Silicon waveguides. *Opt. Expr.* **12,** 2774–2780 (2004).
13. Agrawal, G. P. *Nonlinear Fiber Optics* 2nd edn, 42–43 (Academic, New York, 1995).
14. Jones, R. *et al.* Net continuous wave optical gain in a low loss silicon-on-insulator waveguide by stimulated Raman scattering. *Opt. Expr.* **13,** 519–525 (2005).
15. Siegman, A. E. *Lasers* 413–418 (University Science Books, Mill Valley, 1986).
16. Suto, K., Kimura, T. & Nishizawa, J. Semiconductor Raman laser pumped with a fundamental mode. *IEE Proc. J.* **139,** 407–412 (1992).
17. Brasseur, J. K., Repasky, K. S. & Carlsten, J. L. Continuous-wave Raman laser in H₂. *Opt. Lett.* **23,** 367–369 (1998).
18. Garmire, E. Criteria for optical bistability in a lossy saturating Fabry-Perot. *IEEE J. Quant. Electron.* **QE-25,** 289–295 (1989).
19. Salib, M. *et al.* Silicon photonics. *Intel Technol. J.* **8,** 143–160 (2004).
20. Liu, M. Y. & Chou, S. Y. High-modulation-depth and short-cavity-length silicon Fabry–Perot modulator with two grating Bragg reflectors. *Appl. Phys. Lett.* **68,** 170–172 (1996).
21. Barrios, C. A., Almeida, V. R., Panepucci, R. R., Schmidt, B. S. & Lipson, M. Compact silicon tunable Fabry-Perot resonator with low power consumption. *IEEE Photon. Technol. Lett.* **16,** 506–508 (2004).
22. Headley, W. R., Reed, G. T., Liu, A., Paniccia, M. & Howe, S. Polarization independent optical racetrack resonators using rib waveguide on silicon on insulator. *Appl. Phys. Lett.* **85,** 5523–5525 (2004).
23. Lee, M.-C. M. & Wu, M. C. in *IEEE/LEOS Int. Conf. on Optical MEMS and Their Applications (Hawaii, 18–21 August 2003)* Paper MC3 28–29 (IEEE, Piscataway, NJ, 2003).
24. Koonath, P., Indukuri, T. & Jalali, B. Vertically coupled micro-resonators realized using three-dimensional sculpting in silicon. *Appl. Phys. Lett.* **85,** 1018–1020 (2004).
25. Kippenberg, T. J., Spillane, S. M., Armani, D. K. & Vahala, K. J. Ultralow-threshold microcavity Raman laser on a microelectronic chip. *Opt. Lett.* **29,** 1224–1227 (2004).

Figure 4 Silicon Raman laser spectra. **a**, Measured with a confocal scanning Fabry–Pérot spectrum analyser. Displayed is a scan over one free spectral range of 8 GHz showing single-mode operation of the laser. The measured linewidth of 80 MHz is limited by the resolution of the spectrum analyser. **b**, Measured with a grating-based optical spectrum analyser at different pump wavelengths from 1,548 nm to 1,558 nm in 2-nm steps, showing a side mode suppression of >55 dB.

······························

Biological control of terrestrial silica cycling and export fluxes to watersheds

Louis A. Derry[1], **Andrew C. Kurtz**[2], **Karen Ziegler**[3] & **Oliver A. Chadwick**[3]

[1]*Department of Earth and Atmospheric Sciences, Cornell University, Ithaca, New York 14853, USA*
[2]*Department of Earth Sciences, Boston University, Boston, Massachusetts 02215, USA*
[3]*Department of Geography, University of California, Santa Barbara, California 93106, USA*

....

Silicon has a crucial role in many biogeochemical processes—for example, as a nutrient for marine and terrestrial biota, in buffering soil acidification and in the regulation of atmospheric carbon dioxide. Traditionally, silica fluxes to soil solutions and stream waters are thought to be controlled by the weathering and subsequent dissolution of silicate minerals[1,2]. Rates of mineral dissolution can be enhanced by biological processes[3]. But plants also take up considerable quantities of silica from soil solution, which is recycled into the soil from falling litter in a separate soil–plant silica cycle that can be significant in comparison with weathering input and hydrologic output[4–8]. Here we analyse soil water in basaltic soils across the Hawaiian islands to assess the relative contributions of weathering and biogenic silica cycling by using the distinct signatures of the two processes in germanium/silicon ratios. Our data imply that most of the silica released to Hawaiian stream water has passed through the biogenic silica pool, whereas direct mineral–water reactions account for a smaller fraction of the stream silica flux. We expect that other systems exhibiting strong Si depletion of the mineral soils and/or high Si uptake rates by biomass will also have strong biological control on silica cycling and export.

Germanium/silicon ratios have been used to trace silica sources in rivers and the oceans[9,10]. Ge/Si ratios in streams unaffected by pollution or hydrothermal inputs are always lower than Ge/Si in the silicate bedrock that they drain[11]. Secondary minerals (clays) formed in the soil environment are the major complementary reservoir higher in Ge/Si (refs 12–14). Dissolved Ge–Si relationships from most rivers from a variety of climatic and geological settings are similar, and comprise trends that have been explained as mixing between silica derived from weathering of primary minerals and silica derived from weathering of secondary clays[12,13]. According to this scheme, which we term the Murnane, Stallard, Froelich (MSF) model, incongruent dissolution of primary minerals yields a solution with high Si concentration, [Si], and low Ge/Si (component 1), whereas dissolution of secondary, Ge-enriched clays yields a low-[Si], high-Ge/Si solution (component 2).

The MSF model assumes direct mineralogical control on stream silica (and germanium). According to this model, mineral stability controls the concentrations of dissolved silica in equilibrium with clay assemblages; mineral weathering rates define the available flux of Si; and the degree of dilution of solutions generated in the weathering environment sets overall stream [Si]. Ge/Si ratios in soil solutions should reflect the soil mineral phases undergoing dissolution or transformation[15]. However, the recognition of an active terrestrial biological cycle of Si raises questions about the pathways of silica from weathering to streams. Many plants sequester silica in biogenic phytoliths (opal-A structures), and soils can accumulate significant quantities of biogenic opal-A[16]. What is the impact of this internal plant cycle on stream Si fluxes? Is stream export largely unaffected by this process, or does the 'internal' plant cycle have a significant role in controlling silica export from watersheds?

The Hawaiian islands offer an opportunity to test the predictions of the MSF model and to investigate the impact of biogenic silica cycling on stream export. Ge/Si in fresh Hawaiian basalts (tholeitic and alkaline) fall in a relatively narrow range of $(2.3–2.9) \times 10^{-6}$ (mol/mol) (ref. 17). Ge and Si data from Hawaiian streams unaffected by coal burning or hydrothermal inputs define an apparent mixing relationship[11] (Fig. 1). The data can be modelled as a two-component mixture in which component 1 has Ge/Si $\approx 0.2 \times 10^{-6}$ and [Si] $> 600\,\mu$M, and component 2 has Ge/Si $\approx 2.6 \times 10^{-6}$ and [Si] $\le 25\,\mu$M (Fig. 1). The MSF model predicts that the low-Ge/Si, high-[Si] component 1 is produced during the incongruent dissolution of primary minerals in the lower part of soil profiles, near the interface with fresh material, and/or in the upper parts of young soils that are not yet depleted of silica and retain primary minerals. High-Ge/Si, low-[Si] solutions (component 2) should occur in the upper parts of weathered soil profiles that have lost their primary minerals and in which the dissolution of secondary clays with high Ge/Si is important.

We tested the predictions of the above model by measuring [Ge] and [Si] in soil waters from seven depth profiles along a chronosequence of basaltic soils across the Hawaiian islands. The chronosequence ranges from 0.3 to 4,100 kyr substrate age, but has common rock type, present-day climate and vegetation[18,19]. Major element geochemistry, soil mineralogy and solid-phase Ge/Si ratios have been characterized by previous studies. Young soils (about 0.3 kyr old) retain primary minerals and volcanic glass, have experienced little Si loss, and have Ge/Si ratios close to that of fresh basalt[14]. Older soils (at least 20 kyr old) have experienced
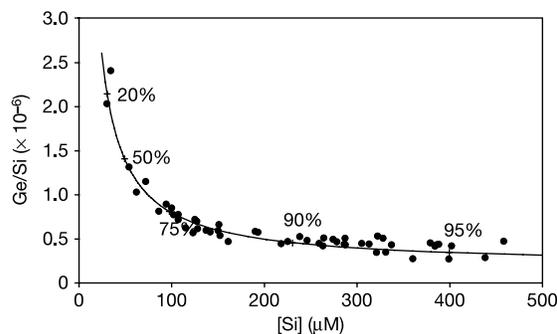

Figure 1 Plot of Ge/Si against [Si] from Hawaiian stream waters. Data are from ref. 12 and this study. The hyperbolic curve is a two-component mixing model, in which component 1 is derived from the dissolution of biogenic silica and has Ge/Si = 0.25×10^{-6} and [Si] = $1,800\,\mu$M, and component 2 is derived from the dissolution of soil minerals and has Ge/Si = 2.6×10^{-6} and [Si] = $25\,\mu$M. Hawaiian streams generally show lower [Si] and higher Ge/Si at high discharge. The discharge-weighted stream fluxes have Ge/Si < 1 and [Si] > $80\,\mu$M, implying that component 1 is the larger contributor of dissolved silica and indicating a major role for biogenic silica in controlling stream Si export. Labelled crosses on the mixing curve indicate the modelled fraction of biogenic Si.